ACS Catalysis

Subscriber access provided by University of Newcastle, Australia

Article

Generation of reactive oxygen species via electroprotic interaction of HO with ZrO gel – ionic sponge effect and pH-switchable peroxidase- and catalase-like activity

Kamila Soba#ska, Piotr Pietrzyk, and Zbigniew Sojka

ACS Catal., **Just Accepted Manuscript** • DOI: 10.1021/acscatal.7b00189 • Publication Date (Web): 14 Mar 2017

Downloaded from http://pubs.acs.org on March 15, 2017

Just Accepted

“Just Accepted” manuscripts have been peer-reviewed and accepted for publication. They are posted online prior to technical editing, formatting for publication and author proofing. The American Chemical Society provides “Just Accepted” as a free service to the research community to expedite the dissemination of scientific material as soon as possible after acceptance. “Just Accepted” manuscripts appear in full in PDF format accompanied by an HTML abstract. “Just Accepted” manuscripts have been fully peer reviewed, but should not be considered the official version of record. They are accessible to all readers and citable by the Digital Object Identifier (DOI®). “Just Accepted” is an optional service offered to authors. Therefore, the “Just Accepted” Web site may not include all articles that will be published in the journal. After a manuscript is technically edited and formatted, it will be removed from the “Just Accepted” Web site and published as an ASAP article. Note that technical editing may introduce minor changes to the manuscript text and/or graphics which could affect content, and all legal disclaimers and ethical guidelines that apply to the journal pertain. ACS cannot be held responsible for errors or consequences arising from the use of information contained in these “Just Accepted” manuscripts.

ACS Catalysis is published by the American Chemical Society. 1155 Sixteenth Street N.W., Washington, DC 20036

Published by American Chemical Society. Copyright © American Chemical Society. However, no copyright claim is made to original U.S. Government works, or works produced by employees of any Commonwealth realm Crown government in the course of their duties.

Generation of reactive oxygen species via electroprotic interaction of H_2O_2 with ZrO_2 gel – ionic sponge effect and pH-switchable peroxidase- and catalase-like activity

Kamila Sobańska, Piotr Pietrzyk, Zbigniew Sojka*

Faculty of Chemistry, Jagiellonian University, ul. R. Ingardena 3, 30-060 Krakow, Poland

ABSTRACT

Formation of reactive oxygen species (ROS) is of vital importance in catalytic oxidation chemistry. In this paper we have shown that a non-redox system such as amorphous zirconium dioxide (*a*-ZrO_2) is highly active in ROS formation via H_2O_2 decomposition. Interaction between *a*-ZrO_2 and H_2O_2 in aqueous solution was investigated by means of EPR, HYSCORE, Raman, UV-Vis, along with auxiliary FTIR, TG-MS, and XPS techniques in a broad range of pH values and H_2O_2 concentrations. Various reaction intermediates such as superoxide ($O_2^{-\bullet}$) and hydroxyl ($^{\bullet}OH$) radicals as well as peroxide (O_2^{2-}) species were identified. At pH below 5.3 the superoxide and hydroxyl radicals were generated simultaneously in large amounts with the peak concentration reached around the isoelectric point of the gel catalyst. In this pH region, the ZrO_2 gel exhibited the peroxidase-type activity, quantified by o-phenylenediamine assay. At pH > 5.3 formation of O_2^{2-} is accompanied by a substantial release of O_2 due to the pronounced catalase-like activity of *a*-ZrO_2. The role of electroprotic processes (an interfacial proton transfer coupled with an intermolecular electron transfer) in H_2O_2 decomposition and ROS formation was elucidated, and a plausible mechanism of this reaction, $\equiv Zr^{+}–HO_2^{-}{}_{(surf)} + H_2O_{2(aq)} \rightarrow {}^{\bullet}OH_{(aq)} + \equiv Zr^{+}–O_2^{-\bullet}{}_{(surf)} + H_2O$, was proposed. The surface of *a*-ZrO_2 covered with hydroxyl groups plays a role of an ionic sponge, which controls the electroprotic equilibrium by capturing the charged reaction intermediates. Unlike amorphous gel, crystalline zirconia exhibits only weak activity in production of the $O_2^{-\bullet}$ and $^{\bullet}OH$ radicals, and different mechanism is involved. It is worth mentioning that the activity of the zirconia gel catalyst in ROS generation, gauged by the Michaelis-Menten constant, is comparable (ca. 40%) to that of the Fenton-type oxides (Fe_3O_4, Co_3O_4).

Keywords

hydrogen peroxide, superoxide, hydroxyl radicals, oxidation catalyst, amorphous zirconia, decomposition mechanisms, HYSCORE

1. Introduction

Due to the increasing use of hydrogen peroxide (H_2O_2) as a cheap and environmentally benign oxidant in many catalytic reactions, extensive studies into mechanisms of H_2O_2 activation (decomposition), and search for new catalysts active in this reaction have recently received a great deal of attention.[1,2,3,4,5,6,7] Hydrogen peroxide is a simple source of reactive oxygen species (ROS) such as $^{\bullet}OH$ (hydroxyl radicals), $O_2^{-\bullet}$ (superoxide radicals), $HO_2^{\bullet}$ (hydroperoxyl radicals) or O_2^{2-} (peroxide anions) of various oxidizing ability.[2,5,8] They can be used in advanced oxidation processes (AOP),[5,9] epoxidation[10] and oxidation[11] of olefins, as well as for catalytic waste water treatment, including removal of organic pollutants exemplified by phenol derivatives.[12] On the other hand, hydroxyl radicals are undesirable species in electrochemical processes such as oxygen reduction reaction (ORR),[13] and for proton conductive fuel cells where they cause chemical degradation of the polymer membranes.[14,15]

The reactive oxygen species (especially $^{\bullet}OH$ radicals) are involved in many biological processes being harmful for living organisms. Because of their kinetic instability, high oxidation potential, and chemical nonselectivity they lead to molecular degradation of cells[16] resulting in extended inflammations. Degradation of protective polymer coatings of medical metal implants by hydroxyl radicals generated upon reaction with transition-metal ions released from the implant surface provides another example of the ROS destructive action.[17]

In catalytic applications, H_2O_2-based oxidation reactions rely on conversion of H_2O_2 into hydroxyl[1,5,12] or superoxide radicals,[18] either by interaction with transition-metal catalysts such as iron and manganese complexes[19] or during photocatalytic processes.[12c] Formation of ROS involves 1-electron reduction of hydrogen peroxide, which in the case of transition-metal catalysts (molecular complexes or oxide surfaces) proceeds according to the Fenton-like mechanism or through processes analogous to those appearing in the Haber-Weiss scheme.[12b]

Other materials active in the 1-electron H_2O_2 reduction are zeolites containing transition-metals and titanium-bearing molecular sieves.[20a] In particular, metallozeolites have been used for partial oxidation of ethane[21] and oxidation of methane to methanol,[22,23] while titanosilicate-1 has been shown to catalyze epoxidation of propylene,[10d] or oxidation of benzene to phenol.[24] Owing to their well-established performance for heterogeneous oxidation of organic substrates, the Ti-based materials may also serve as useful model systems for mechanistic studies.[20a-d] Another route of H_2O_2 activation, but without interfacial electron transfer (non-Fenton pathway) takes place on the surface of d^0 transition-metal ion oxides (*e.g.* ZrO_2, Nb_2O_5, Ta_2O_5) which possess a non-redox character.[5] Such oxides exhibit high activity in glycerol oxidation by H_2O_2.[25]

In particular, the non-Fenton type of H_2O_2 activation has been intensively investigated over crystalline ZrO_2 of the micrometric grain size.[26,27,28] The postulated reaction mechanism consists of three stages

$$H_2O_2 \rightarrow 2{}^{\bullet}OH, \qquad (1)$$

$$^{\bullet}OH + H_2O_2 \rightarrow HO_2^{\bullet} + H_2O, \qquad (2)$$

$$2HO_2^{\bullet} \rightarrow H_2O_2 + O_2, \qquad (3)$$

and does not involve any charged intermediates. The reaction is initiated by the homolytic splitting of H_2O_2 on the surface, leading to the formation of the hydroxyl radicals (Equation 1). The latter interacting with H_2O_2 produce hydroperoxyl species (Equation 2). Accumulation of $HO_2^{\bullet}$ radicals in solution leads to their bimolecular decomposition into H_2O_2 and dioxygen (Equation 3). Similar mechanism has been proposed for aqua complexes of M^{3+} ions (M = Ga, In, Sc, Y, La),[29] for which formation of $^{\bullet}OH$ is again associated with their ability to the homolytic cleavage of the HO–OH bond.

Enzymatic abatement of undesired hydrogen peroxide in biological systems occurs along two basic pathways referred to as *activity of peroxidase*,

$H_2O_2 + e^- + H^+ \rightarrow {}^{\bullet}OH + H_2O$ followed by ${}^{\bullet}OH + e^- + H^+ \rightarrow H_2O$; (4)

and *activity of catalase,* where hydrogen peroxide is “directly” decomposed into dioxygen

$H_2O_2 \rightarrow H_2O + ½\ O_2$. (5)

In the case of the peroxidase activity the necessary electrons and protons are provided by a donor molecule (RH), giving rise to the following overall reaction: $H_2O_2 + 2R–H \rightarrow 2H_2O + R–R$. The characteristic feature of the peroxidase pathway is formation of hydroxyl radical intermediates in the course of the reaction, in contrast to the catalase-like activity, which does not involve explicit ROS formation.[30] The systems capable of peroxidase-like activity can also be used as electrochemical sensors for detection of H_2O_2 with great sensitivity, and an example is provided by ZrO_2-grafted collagen scaffold with adsorbed horseradish peroxidase.[31] There are several inorganic compounds (often referred to as inorganic mimetics of catalase and peroxidase) exhibiting similar reactivity patterns as those of the enzymes. Examples of the peroxidase mimetics are provided by TiO_2 nanotubes,[32] Co_3O_4 nanoparticles,[33] Fe_3O_4,[1,34] V_2O_5 nanowires,[35] CeO_2,[36] or FeS.[37] They produce ROS detectable by means of specific substrates such as TMB (3,3’,5,5’-tetramethylbenzidine), OPD (ortho-phenylenediamine) or ABTS (2,2’-azino-bis(3-ethyl-benzthiazoline-6-sulfonic acid), which selectively react with the ${}^{\bullet}OH$ radicals.[38] Superoxide radicals ($O_2^{-\bullet}$), in turn, can be measured with nitro blue tetrazolium (NBT) substrate and UV-vis detection.[39] Another technique, which is helpful in observation of both ${}^{\bullet}OH$ and $O_2^{-\bullet}$ radicals, is electron paramagnetic resonance spectroscopy (EPR) alone and in tandem with using 5,5-dimethyl-1-pyrroline-N-oxide (DMPO) as a spin trap.[40]

Unlike the previous studies concerning only a crystalline state of ZrO_2, in this work we describe application of amorphous zirconia gel for profuse generation of ROS via H_2O_2 decomposition, by exploiting its pH-tunable peroxidase- and catalase-like reactivity. The observed simultaneous appearance of $^{\bullet}OH$ and $O_2^{-\bullet}$ species, which cannot be accounted for within the previously proposed radical mechanisms, indicates that the respective reaction steps reported in literature have to be carefully revisited while explaining the activity of the gel catalyst. For this purpose, the influence of the isoelectric point, pH of the reaction mixture, and the crystallinity degree of the zirconia catalyst on ROS formation and speciation was examined by means of *in situ* EPR/HYSCORE, UV-vis, Raman, TG-MS, and XPS spectroscopies, corroborated by spin trapping and dissolved O_2 measurements, as well as the test reactions for peroxidase-like activity with OPD and NBT substrates. The results were accounted for by a new electroprotic mechanism of H_2O_2 activation, where an ionic sponge comportment of the zirconia gel plays a crucial role. Because the peroxidase-type activity of the zirconia gel may be regarded as a measure of generation of $^{\bullet}OH$ radicals that can be used for the oxidation processes, and the catalase-like activity corresponds to that part of H_2O_2 which is virtually lost by immediate decomposition into O_2, a diagram showing preferable conditions for the catalytic oxidation processes involving H_2O_2 was proposed. To our knowledge, this is the first example of a mechanistic study of such type of the interfacial chemistry between hydrogen peroxide and d^0 metal oxide gels.

2. Materials and Methods

2.1. Materials. Amorphous zirconia (*a*-ZrO_2) powder was prepared from analytically pure $ZrOCl_2 \cdot 8H_2O$ that was dissolved in distilled water. Subsequently, 25% ammonia solution was added drop-wise under vigorous stirring. The precipitate was washed with distilled water until a negative reaction for Cl^- ions, and dried at room temperature. For the spectroscopic characterization of solid samples (EPR, Raman, XPS, TG-MS) typically 0.1 g of the catalyst was treated with 1.35 mL of hydrogen peroxide (Sigma Aldrich) aqueous solution of various concentrations (5 – 30%). This treatment was performed at room temperature by gradual addition of H_2O_2 solution. The pH level was adjusted using 0.1M NH_3 or 0.1M HCl aqueous solutions. The resulting samples were dried at room temperature. As a reference sample, a commercial crystalline *m*-ZrO_2 (Sigma Aldrich) of the monoclinic structure with the grain size of ~5 μm was used.

2.2. Reactions. The peroxidase-like activity of the amorphous zirconia was investigated by measuring absorbance of the oxidation product of the peroxidase substrate, OPD, with $^{\bullet}OH$ radicals. The experiments were carried out using suspensions composed of 1.3 mg/mL of *a*-ZrO_2 with 1.2 mmol/L OPD as a substrate, and 0.3 mol/L of H_2O_2. Whereas for colorimetric detection of the produced superoxide radicals NBT was applied as a specific reagent (4 mmol/L). The reactions were followed by means of a Cary 60 UV-Vis spectrophotometer (Agilent Technologies), and the spectra were recorded with elapsing time in the range of 200 – 800 nm.

The hydroxyl and superoxide radicals generated in the liquid phase were additionally detected by applying the spin trapping technique. DMPO (Sigma Aldrich) was chosen as a suitable spin trap because of its well documented high trapping ability and selectivity toward oxygen-centered radicals.[40] In the spin-trapping experiments a small amount of ZrO_2 was contacted with a mixture of 1 mL of H_2O_2/H_2O and 10 μL of DMPO. The liquid sample was next transferred into a quartz capillary, and the EPR spectra were recorded at room temperature.

2.3. Physicochemical Methods. Continuous wave EPR spectra were recorded with an X-band Bruker ELEXSYS-II E580 spectrometer, operating at 100 kHz field modulation with the 0.1 – 0.5 mT modulation amplitude. The spectra of the gel part of the samples were measured at 77 K, whereas the liquid component was measured at ambient temperature. Prior to the measurements, the samples (10 mg) were sealed in quartz tubes and outgassed in a vacuum line ($p < 10^{-3}$ mbar) for 2h at room temperature. The EPR parameters of the resultant paramagnetic species were determined by computer simulation of the experimental spectra using the EPRsim32 package.[41]

Pulse EPR experiments were performed at the microwave frequency of 9.68 GHz at 40 K (Oxford Instruments LHe cryostat). Electron spin echo (ESE) detected EPR experiments were carried out based on the pulse sequence of $\pi/2$–τ–π–τ–echo, with the microwave pulse lengths $t_{\pi/2}$ = 16 ns, t_{π} = 32 ns, and the τ value of 200 ns. Hyperfine sublevel correlation (HYSCORE) measurements were carried out using the pulse sequence of $\pi/2$–τ–$\pi/2$–t_1–π–t_2–$\pi/2$–τ–echo, with the microwave pulse lengths $t_{\pi/2}$ = 16 ns and t_{π} = 16 ns. In order to avoid blind spot effects, different τ values were used, as specified in the figure captions. In order to enhance the ^{1}H superhyperfine signal and the resulting correlation ridges due to the specifically interacting surface protons, the matched HYSCORE experiments were performed with high-turning angle (HTA) pulses incorporated into the pulse sequence $\pi/2$–τ–HTA–t_1–π–t_2–HTA–τ–echo. The optimal length of the HTA pulse of 80 ns was determined experimentally. More details about pulse experiments can be found in Supporting Information. The obtained correlation spectra were simulated with the EasySpin software.[42]

Diamagnetic ROS varieties were detected by Raman spectroscopy. The measurements were performed at ambient conditions with a Renishaw InVia dispersive spectrometer quipped with a CCD detector and integrated with a Leica DMLM confocal microscope. Two laser lines (785 nm and 514 nm) were used depending on the observed signal intensity. The Raman scattered light was collected with a 50x Olympus objective in the spectral range of 100 – 1500 cm^{-1}. Nine scans were accumulated to assure a good signal-to-noise ratio.

FTIR spectra were recorded with Nicolet 6700, Thermo Scientific, spectrophotometer using a single reflection ATR device with a diamond crystal. Powder X-ray diffraction (XRD) measurements were performed by means of a Rigaku MiniFlex 600 diffractometer equipped with a D/teX high speed silicon strip detector and a 600 W X-ray source (Cu $K\alpha_1$ radiation).

The zeta potential as a function of pH, and the isoelectric point (IEP) were measured by means of a Zetasizer Nano ZS apparatus (Malvern), equipped with a 633 nm laser and combined with a MPT-2 auto-titrator. The suspension was titrated with either 0.1 M NaOH or HCl. The zeta potential value was calculated from the electrophoretic mobility by applying the Smoluchowski equation.

The concentration of dissolved oxygen was monitored *in situ* with an inoLab Multi 9430 IDS setup, equipped with an optical sensor FDO 925 (WTW). The sensor was immersed in the *a*-ZrO_2/H_2O_2 suspension, and the concentration of the evolving O_2 was monitored as a function of time and pH of the solution, while keeping the temperature constant at $T = 295$ K.

The X-ray photoelectron spectra (XPS) were recorded on a Prevac photoelectron spectrometer equipped with a hemispherical VG SCIENTA R3000 analyzer. The spectra were measured using a monochromatized aluminum AlK_α source ($E = 1486.6$ eV). A low energy electron flood gun (FS40A-PS) was used to compensate the surface charge. The background pressure in the analytical chamber during the measurements was equal to 5×10^{-9} mbar. The spectra were recorded with constant pass energy of 100 eV. The binding energies were referenced to the C 1s core level (E_b = 285.0 eV). Fitting of the O 1s and Zr 3d spectra was performed with the CasaXPS software.

Thermogravimetric analysis combined with mass spectrometry detection (TG-MS) was performed using a Mettler Toledo TGA/SDTA 851^e apparatus. The evolving gas products were identified using a ThermoStar GSD300T Balzers quadruple mass spectrometer (QMS) operated in the selected-ion monitoring (SIM) mode. To monitor O_2, H_2O and H_2O_2 (and their fragmentation products) the following masses (*m*/*z*) were recorded: 17, 18, 32, 33 and 34. The measurements were carried out in a flow of argon (80 $cm^3 \cdot min^{-1}$) in the temperature range 290 – 1073 K, at a constant heating rate of 3 $K \cdot min^{-1}$.

3. Results and Discussion

Interaction of an aqueous solution of H_2O_2 with amorphous zirconia led to the formation of both the liquid-phase and the surface-trapped reactive oxygen species. The surface ROS were analyzed by XPS, Raman, EPR, and TG-MS techniques, whereas liquid-phase radicals were detected by EPR spectroscopy, applied in tandem with the spin trapping technique, and UV-vis colorimetric measurements using OPD substrate. The peroxidase- or catalase-like activity of the amorphous ZrO_2 was next evaluated as a function of pH by measuring the amount of the hydroxyl radicals (OPD substrate assay) and dissolved oxygen, respectively.

3.1. Oxygen species trapped on *a*-ZrO_2 surface

Accumulation of the oxygen species on the surface upon interaction of H_2O_2 aqueous solution with *a*-ZrO_2 was revealed by XPS spectra, recorded in the 542 – 525 eV region, before (Figure 1a) and after (Figure 1b) the reaction. The observed multicomponent O 1s band was disentangled by a least-squares fitting, assuming the contributions from four distinct signals corresponding to adsorbed H_2O (536 eV), adsorbed oxygen species (534 eV), surface Zr–OH groups (531.5 eV) and lattice O^{2-} anions (530.3 eV).[43] The results indicate clearly a substantial increase in the amount of the adsorbed oxygen species (yellow-shaded signal in Figure 1) upon the interaction with H_2O_2, as the area of the 534 eV peak increased from 10% to 18% of the total intensity of the O 1s band. At the same time the component due to the surface hydroxyls (green area in Figure 1) augmented from 37% to 42%. In the Zr 3d region (Figure S1) virtually no changes in the XPS spectra were observed for the pristine and the H_2O_2-treated samples.

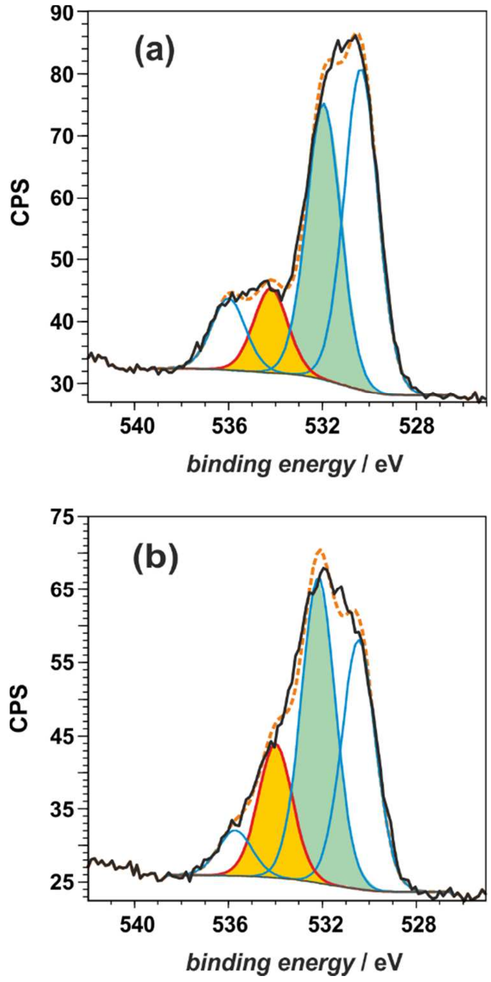

Figure 1. XPS spectra recorded in the O 1s region for *a*-ZrO_2 (a) before and (b) after the reaction with 30% H_2O_2, along with decomposition of the oxygen band into the individual component signals (yellow area – adsorbed oxygen species, green area – surface hydroxyl groups).

The XPS results show that after the reaction with hydrogen peroxide the surfaces of the dried amorphous zirconia gel is covered simultaneously by the adoxygen, hydroxyls, and adsorbed water. The chemical nature of the adoxygen species unraveled by XPS was next examined by Raman and EPR measurements.

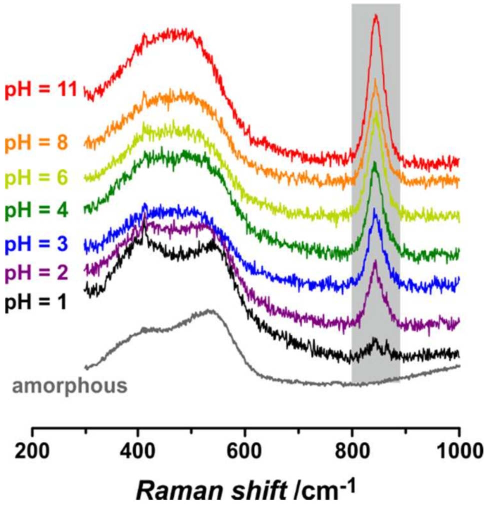

Figure 2. Raman spectra of amorphous ZrO_2 treated with H_2O_2 at various pH. The shadowed region around 840 cm^{-1} is diagnostic of the surface peroxo (O_2^{2-}) species.

Raman spectra of the H_2O_2-treated zirconia gel at pH ranging from 1 to 11 (Figure 2) show a band located at 841 cm^{-1} assigned to the O–O vibration of surface peroxo species[44] (a similar band was observed for peroxo species bound to zirconia-based oxoclusters).[45] Such attribution is in agreement with the observed changes in the intensity of this band with respect to pH of the reaction mixture. It increases significantly with the increasing pH (upon addition of $NH_{3(aq)}$), which can be accounted for by forced dissociation of H_2O_2 into peroxo species that are next captured on the zirconia surface (see discussion below).

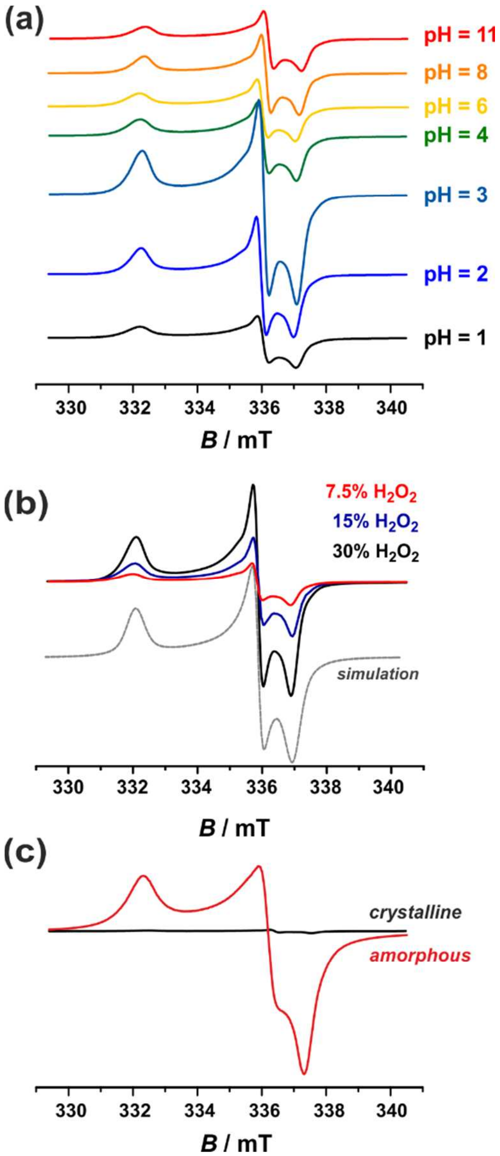

Figure 3. Powder EPR spectra (recorded at 77 K) of *a*-ZrO_2 (a) treated with hydrogen peroxide at various pH and (b) of various H_2O_2 concentrations, (c) comparison of superoxide signals observed for amorphous and crystalline ZrO_2 samples. Gray dashed line represents corresponding simulated spectrum.

Complementary EPR measurements of the *a*-ZrO_2 treated with H_2O_2 solution at various pH were subsequently performed. The obtained orthorhombic signal (Figure 3a), observed upon drying of the samples, is characteristic of the surface-stabilized superoxide anions.[26,46] The intensity of the $O_2^{-\bullet}$ signal changes strongly with the acidity of the reaction medium (Figure 3a) and the concentration of H_2O_2 as well (Figure 3b), but its symmetry and shape are essentially preserved. Whereas for the increasing H_2O_2 concentration the intensity of the $O_2^{-\bullet}$ signal grows steadily, in the case of pH-dependent measurements a clearly non-monotonous variation of the EPR intensity was observed, with a maximum appearing at pH around 3. The mechanistic significance of these observations is discussed below.

The spin-Hamiltonian parameters of the observed EPR signal, $g_{xx} = 2.0029$, $g_{yy} = 2.0095$, and $g_{zz} = 2.0329$, obtained by computer simulation, are typical of the superoxide ions stabilized electrostatically on the surface Zr(IV) centers.[26,46] On the contrary to the amorphous zirconia, for the crystalline *m*-ZrO_2 specimen the EPR signal due to $O_2^{-\bullet}$ is barely visible (Figure 3c), reaching up to 1.6% of the intensity obtained for the amorphous system, indicating that the crystallinity of zirconia plays an important role in the interaction with H_2O_2 that leads to the formation of superoxide species. Similar EPR signals were observed previously for crystalline monoclinic zirconia.[26]

To unravel the role of zirconia crystallinity in the activation of hydrogen peroxide in a more detail, we studied formation of the superoxide radicals over a series of ZrO_2 samples of gradually decreasing BET surface area (Figure 4a), obtained by calcination of the parent zirconia gel at progressively increasing temperatures (298 – 873 K). The EPR measurements show that the intensity of the $O_2^{-\bullet}$ signal declines sharply with the decreasing surface area of the zirconia sample (Figure 4a). However, by plotting the normalized EPR signal intensity (I_{EPR}) with respect to the surface area (S_{BET}) as a function of the calcination temperature (Figure 4b), it can be observed that this ratio exhibits a sigmoidal shape, falling abruptly around 500 K. Such behavior indicates that not only a mere surface area itself, but also the concomitant changes in the chemical nature of the surface induced by the calcination are of crucial importance for the observed depletion of the trapped superoxide species.

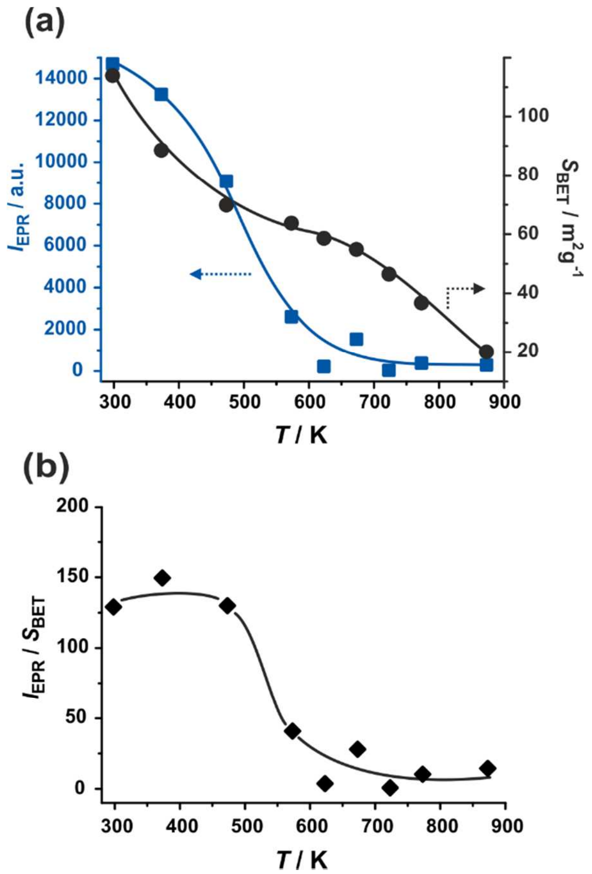

Figure 4. (a) Influence of calcination temperature of *a*-ZrO_2 sample on EPR signal intensity (I_{EPR}) of superoxide species and BET surface area (S_{BET}). (b) Variation of the I_{EPR}/S_{BEA} ratio with increasing calcination temperature.

The implied chemical changes involve dehydroxylation and dehydration of the surface, as shown by the IR spectra of the OH vibration region (Figure 5a), followed by phase transformation from an amorphous gel into a mixture of the monoclinic and tetragonal polymorphs of zirconia, determined by XRD measurements (Figure 5b). The obtained results show the importance of the Zr–OH groups for seizing the superoxide anions on the surface of the zirconia gel in large amounts.

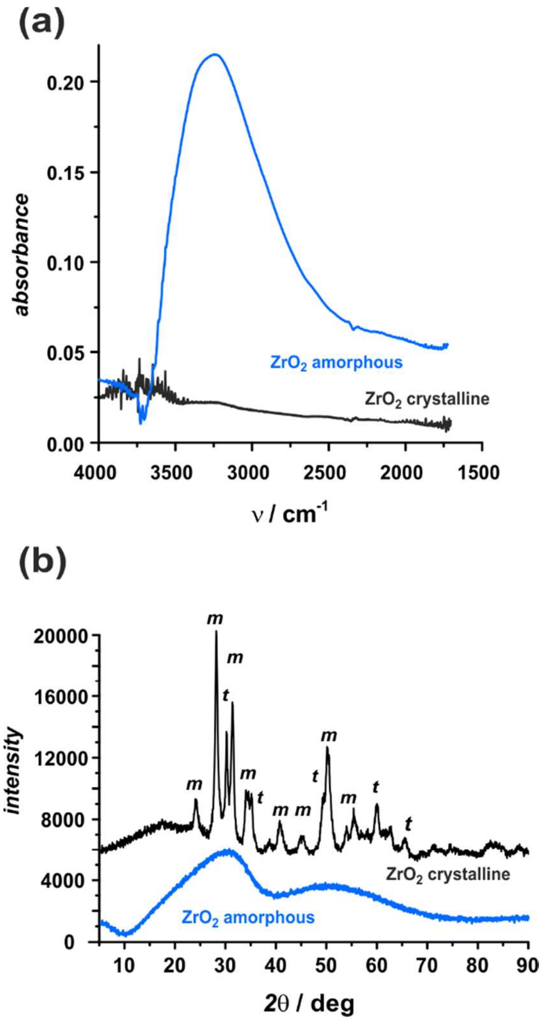

Figure 5. (a) FTIR ATR spectra and (b) powder XRD patterns of amorphous and crystalline ZrO_2 samples (calcination at 773 K in air). *t* indicates a tetragonal phase, and *m* a monoclinic phase of ZrO_2.

To probe the chemical environment (surface OH groups) of the superoxide species adsorbed on the *a*-ZrO_2 surface in more detail, pulse EPR measurements were carried out. At the beginning, an electron spin echo (ESE) detected EPR spectrum was recorded (Figure S2a, Supporting Information), the first derivative of which closely resembles the corresponding CW-EPR spectrum shown in Figure 3. The ESE spectrum was used for selection of the magnetic field observer positions (B_1, B_2, and B_3), corresponding to the principal orientations of the $\boldsymbol{g}$ tensor at which the HYSCORE experiments were then performed.

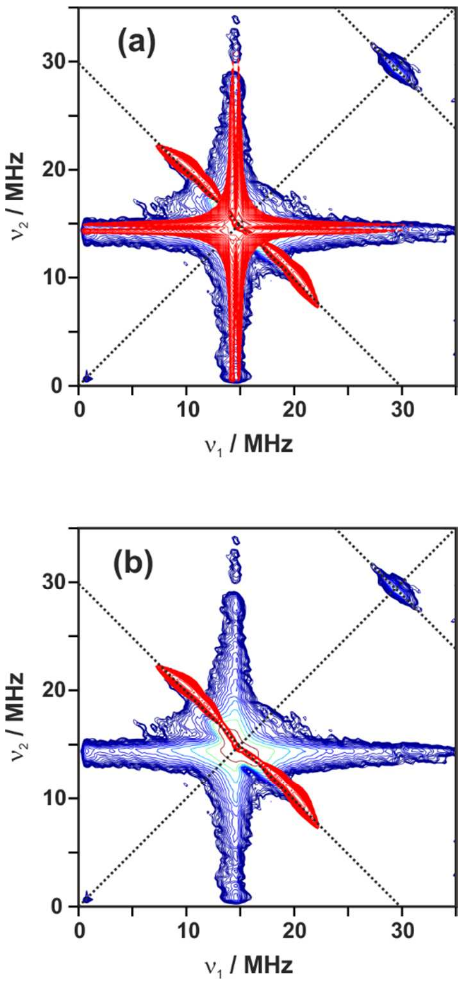

Figure 6. HYSCORE spectra taken at magnetic field of B_2 = 344.2 mT with τ = 128 and 176 ns. The red patterns represent computer simulation results, where (a) the matrix effect resulting from

remote protons due to the surface Zr–OH and H_2O adspecies was included along with the specifically interacting protons, (b) only one type of the protons coupled via superhyperfine interaction with the superoxide species was considered.

An exemplary 2D matched HYSCORE spectrum recorded for the B_2 observer position is shown in Figure 6. The spectrum is featured by a singular correlation peak with the major intensity at (14.6, 14.6) MHz, corresponding to the ^{1}H Larmor frequency (ν_H) at 344.2 mT.[47] This type of signal (present for all the observer positions B_1, B_2 and B_3 shown in Figure S2b,c,d, Supporting Information) originates from the abundant remote protons due to the surface Zr–OH and H_2O adspecies, forming a matrix effect (see simulation in Figure 6a). It tends to suppress the signal originating from the presence of the proximal protons interacting with the superoxide species explicitly, revealed by the simulation (Figure 6b). The superhyperfine interaction (gauged by the $A_{iso} + [-T, -T, 2T]$ tensor) with the proximal protons ($S = 1/2$ and I (^{1}H) = 1/2) gives rise to the appearance of ridges (extended correlation peaks due to powder nature of the samples), clearly seen in the (+,+) quadrant of the HYSCORE spectrum. This is indicative of a weak coupling regime $|A_{iso}| < 2\nu_H$, and the shape of the ridge suggests that $|A_{iso}| > |T|$.[48] Additionally, the presence of a signal near $2\nu_H$ frequency (29 MHz), stemming from the double-quantum nuclear coherence,[47,49] indicates that there are at least two proximal protons with moderate couplings to the superoxide species. The upper limit of the superhyperfine coupling parameters, $A_{iso} = 16 \pm 2$ MHz and $T = -1 \pm 0.3$ MHz, was assessed by extensive computer simulations. Within the dipole model approximation, the obtained T value corresponds to the distance of 4.3 ± 0.5 Å, where the protons around the $O_2^{-\bullet}$ species can be located. We may then conclude that the superoxide radical is trapped on the surface Zr(IV) centers and interacts with the surface hydroxyls located in the vicinity of the adsorption center. There are also abundant protons situated beyond the estimated distance limit. A plausible structure of such superoxide environment is shown in Scheme 1.

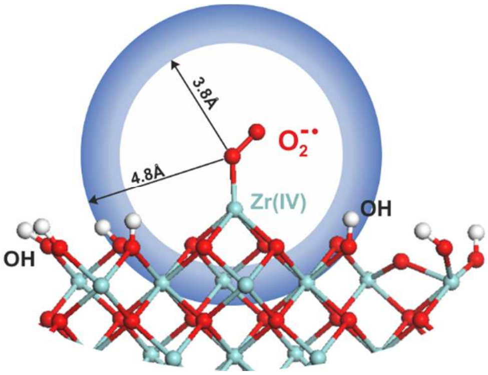

Scheme 1. Structural model of the intimate environment of a superoxide radical anion trapped on the surface of *a*-ZrO_2. The model was generated with Materials Studio (Biovia), structural parameters were taken from ref. [50]: average Zr–O distance 2.2 Å, Zr–O_2^- distance 1.9 Å, Zr–OH 2.08 Å, O–H 1 Å. The arrows show the shortest and the longest $O_2^{-\bullet}$–HO distance calculated based on HYSCORE data.

Thermal stability of the oxygen species accumulated on the *a*-ZrO_2 surface upon interaction with hydrogen peroxide at autogenous pH = 3 (the equilibrium value obtained after mixing up the gel and the H_2O_2 solution) was examined by TG measurements combined with QMS identification of the evolving gas products. The corresponding mass loss profile is shown in Figure 7a. In the temperature range of 300 – 1100 K the observed 29.5% mass loss with the maximum around 350 K (see the $m/z = 17$ signal in Figure 7b), following our previous paper,[51] results mainly from cooperative processes of dehydration ($[Zr_4O_{(8-x)}(OH)_{2x}\cdot yH_2O]_n \rightarrow [Zr_4O_{(8-}$

$_{x)}(OH)_{2x}]_n$ + ynH_2O) and dehydroxylation ($[Zr_4O_{(8-x)}(OH)_{2x}]_n \rightarrow 4n(m/t\text{–}ZrO_2) + xnH_2O$) of the amorphous zirconia.

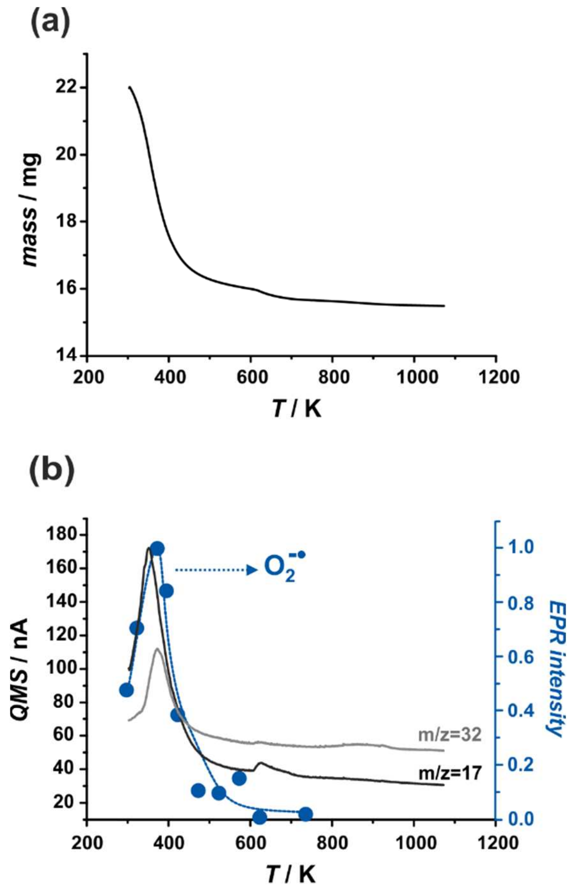

Figure 7. Thermal decomposition of *a*-ZrO_2 after treatment with H_2O_2 at pH = 3. (a) TG profile and (b) QMS signals of H_2O (m/z = 17) and O_2 (m/z = 32) evolving into gas phase during decomposition along with parallel evolution of the EPR signal due to surface superoxide species.

At temperatures around 373 K the surface trapped ROS produced upon interaction with H_2O_2 are decomposed, leading to a release of gaseous O_2 (see the m/z = 32 signal in Figure 7b). The temperature variation of the O_2 evolution matches quite well the corresponding intensity changes in the EPR signal due to the surface superoxide species. Interestingly, it also correlates with the m/z = 17 profile of the desorbed water, indicating that ROS recombination into O_2 may be associated with the surface H_2O discharge. As a result, the concerted changes in the intensities of both the QMS and EPR signals indicate that the surface superoxides formed initially during the reaction between H_2O_2 and *a*-ZrO_2 at ambient temperature become unstable while heating above 330 – 350 K. Large amounts of desorbed O_2 indicates that the charged oxygen species (O_2^- and O_2^{2-}) can only be accommodated on the surface in the presence of charge balancing protons attached to the hydroxyl groups ($\equiv Zr–OH_2^+$). The observed concomitant desorption of H_2O and O_2 implies a mechanism involving superoxide disproportionation, $O_2^{-\bullet}{}_{(surf)} + O_2^{-\bullet}{}_{(surf)} \rightarrow O_{2(g)} + O_2^{2-}{}_{(surf)}$, coupled with thermal dehydration of the surface, $2(\equiv Zr–OH_2^+{}_{(surf)}) + O_2^{2-}{}_{(surf)} \rightarrow \equiv Zr–O–Zr\equiv_{(surf)} + ½O_{2(g)} + 2H_2O$. The implied superoxide disproportionation and O_2 release has been observed previously for, *e.g.*, MoO_x/SiO_2 system.[52] Thus, large amounts of negatively charged O_2^- and O_2^{2-} species accommodated on the gel surface, revealed by thermal desorption, XPS, EPR, and RS investigations are made possible by simultaneous protonation of the surface ($–OH_{(surf)} + H^+{}_{(aq)} \rightarrow –OH_2^+{}_{(surf)}$ and $–O^-{}_{(surf)} + H^+{}_{(aq)} \rightarrow –OH_{(surf)}$), in order to preserve overall charge neutrality within the interfacial layer of the dried gel.

3.2. ROS detected in aqueous phase – hydroxyl radicals

Apart from identification of ROS accumulated on the *a*-ZrO_2 gel upon H_2O_2 treatment, the radicals generated in the aqueous phase of the suspension were determined *in situ* by applying DMPO spin-trap technique and the EPR measurements. After addition of *a*-ZrO_2 gel to the H_2O_2/H_2O mixture, and subsequent separation of the solid phase, an isotropic quartet EPR spectrum characteristic of the DMPO adducts with $^\bullet OH$ radicals was recorded (Figure 8a). The spin-Hamiltonian parameters of the DMPO–$^\bullet OH$ adduct obtained by computer simulation (g_{iso} = 2.0057, a_N = 1.51 mT, a_H = 1.45 mT) remain in a good agreement with the literature data,[40] confirming definitely the presence of $^{\bullet}OH$ radicals in the liquid phase. Blank experiments, carried out at the same conditions but without *a*-ZrO_2 added, showed that no EPR signal was formed (green line in Figure 8a). Parallel EPR measurements of the separated gel revealed a signal that is characteristic of the already observed superoxide species with $g_{xx} = 2.0029$, $g_{yy} = 2.0095$, and $g_{zz} = 2.0329$ (Figure 8b). It was contaminated by a triplet signal due to the nitrosyl radicals, arising from partial degradation of DMPO trap. For the slurry sample, where both the solid *a*-ZrO_2 and the liquid (H_2O_2/H_2O) phases were present together, the EPR signals characteristic of the surface superoxide species ($\equiv Zr(IV)–O_2^{-}{}_{(surf)}$) and the liquid phase hydroxyl radicals ($DMPO–{}^{\bullet}OH_{(aq)}$ adduct) were observed simultaneously (Figure 8c).

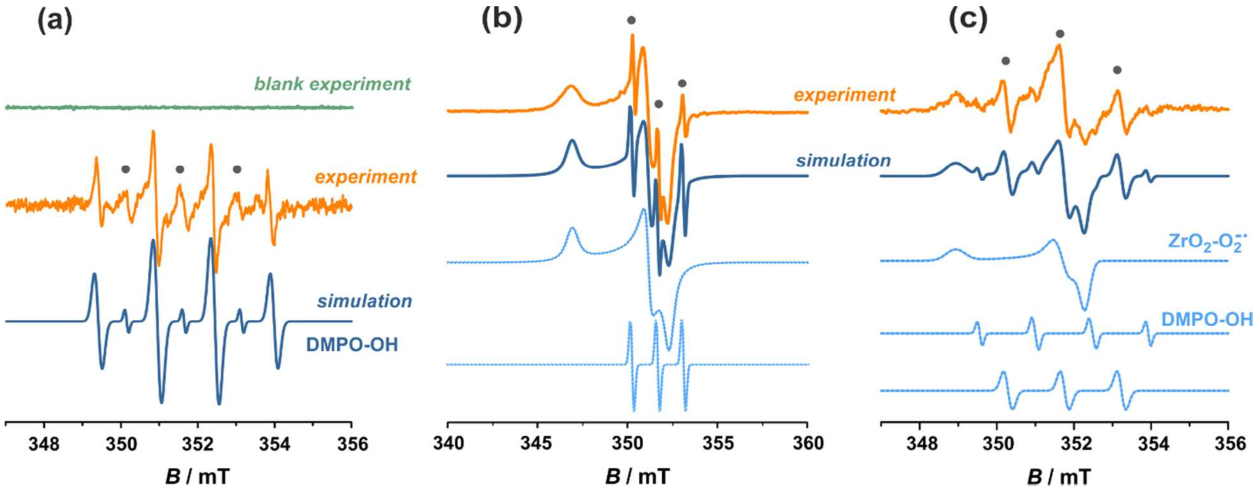

Figure 8. Experimental and simulated EPR spectra recorded at room temperature after the reaction of *a*-ZrO_2 with H_2O_2 in the presence of DMPO spin trap. (a) EPR spectrum of the liquid phase separated from the catalyst, (b) spectrum of the solid *a*-ZrO_2 phase, (c) spectrum of the slurry (*a*-ZrO_2 suspension in H_2O_2/H_2O solution) with the features of the adsorbed superoxide species and $DMPO–{}^{\bullet}OH$ adducts present simultaneously. The nitroxide degradation product of

the spin trap is indicated by gray dots. The simulated EPR signals of particular components are shown as dotted lines.

Apparently, among both types of the simultaneously generated radicals, $O_2^{-\bullet}$ and $^{\bullet}OH$, only the neutral hydroxyl radicals were trapped with DMPO, while within the experimental detection limit, essentially all the charged superoxide species were effectively captured at the surface of *a*-ZrO_2 gel sponge, and additionally stabilized by the surface protons as shown by HYSCORE and XPS measurements.

3.3. The pH dependence of $O_2^{-\bullet}$ vs O_2^{2-} formation

As described above, the amount of the surface peroxide (Figure 2) and superoxide anions (Figure 3a) changes strongly with pH of the reaction mixture. This observation suggests that ROS generation is mediated by protons and their relocation between the solution and the gel surface. Indeed, the pH value of the suspension may influence speciation into the peroxo and superoxo entities by controlling the protic equilibria between the surface (hydroxyls) and liquid phase (H_2O_2/H_2O) components of the suspension. For the pH values below the isoelectic point, IEP = 4.1, (see Figure S3, Supporting Information), the surface of the amorphous zirconia becomes positively charged

$$\equiv Zr\text{–}OH_{(surf)} + H_3O^+_{(aq)} \rightarrow \equiv Zr\text{–}OH_2{}^+_{(surf)} + H_2O, \qquad (6)$$

where $\equiv Zr\text{–}OH_{(surf)}$ should be regarded as surface OH^- group attached to a low coordinated $\equiv Zr(IV)^+$ surface species exhibiting a formal charge of +1 with respect to the fully coordinated Zr(IV) cation. Surface protonation (Equation 6) competes with surface condensation and complexation reactions (owing to the well-known dissociation process $\equiv Zr\text{–}OH_{(surf)} \rightarrow \equiv Zr^+_{(surf)} + OH^-_{(aq)}$),[53] similar to those previously proposed for titania:[54]

$\equiv Zr{-}OH_{(surf)} + H_2O_{2(aq)} \rightarrow \equiv Zr^{+}{-}HO_2^{-}{}_{(surf)} + H_2O,$

(condensation reaction) (7)

$\equiv Zr^{+}{}_{(surf)} + \equiv Zr{-}OH_{(surf)} + H_2O_{2(aq)} \rightarrow \equiv Zr^{+}{-}HO_2^{-}{}_{(surf)} + \equiv Zr{-}OH_2^{+}{}_{(surf)}.$

(complexation reaction) (8)

For pH > 4.1 the surface of *a*-ZrO_2 is negatively charged due to deprotonation of the $\equiv Zr{-}OH_{(surf)}$ groups ($\equiv Zr{-}OH_{(surf)} + OH^{-}{}_{(aq)} \rightarrow \equiv Zr{-}O^{-}{}_{(surf)} + H_2O$), thus, the dissociation of H_2O_2 is controlled by the $OH^{-}{}_{(aq)}$ anions in the liquid phase and the ability of seizing the resultant anions by the gel surface.

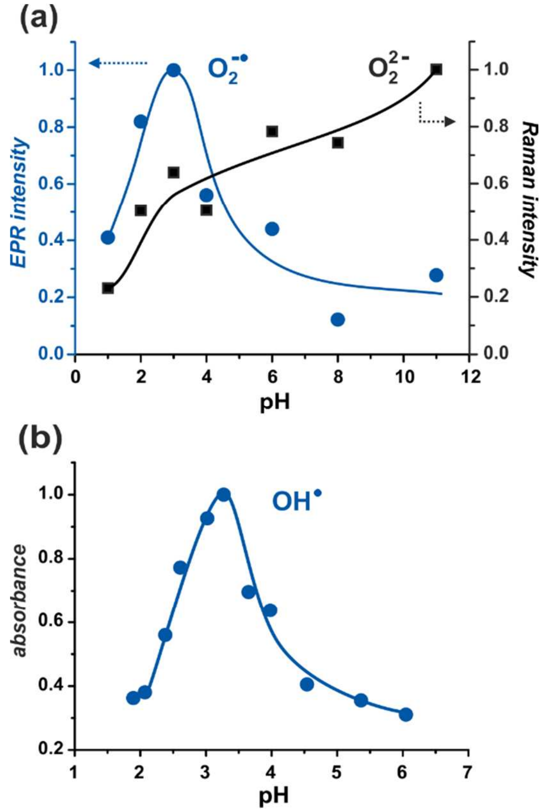

Figure 9. Impact of solution pH on the formation of (a) $O_2^{-\bullet}$ (relative intensity of the EPR spectra) versus O_2^{2-} (relative intensity of the Raman band) species and (b) $OH^{\bullet}$ radicals (changes in the UV-Vis absorbance at 440 nm in the presence of OPD) during the interaction between *a*-ZrO_2 and H_2O_2 solution.

Figure 9 shows variation in the intensity of the spectral signatures of the superoxo and peroxo species, produced during interaction of hydrogen peroxide with *a*-ZrO_2 as a function of pH in more detail. The maximum of the intensity of the superoxide EPR signal is located in the vicinity of the isoelectric point of *a*-ZrO_2 (Figure 9a). An increase or decrease of the pH value in this region results in a rapid drop of the concentration of the surface superoxo radicals. At the same time the concentration of the surface peroxo species increases steadily with pH and both curves ($O_2^{-\bullet}$ and O_2^{2-}) cross slightly above the IEP value. We have recently observed the same IEP-dependent trends in the $O_2^{-\bullet}$ and O_2^{2-} formation for Nb_2O_5 and Ta_2O_5 gels.[5] Indeed, the maximum of the EPR signal intensity for $\equiv Zr^{+}–O_2^{-\bullet}$ is shifted toward higher pH, in agreement with the higher value of the isoelectric point of ZrO_2 as compared to Nb_2O_5, (IEP = 2.8 for amorphous Nb_2O_5 and 4.1 for amorphous ZrO_2). Thus, such behavior is more general in nature, and specific shape of the $([O_2^{-\bullet}], [O_2^{2-}]) = f(\mathrm{pH})$ dependence is characteristic of a given amorphous oxide.

The identified ROS varieties produced during interaction of H_2O_2 with *a*-ZrO_2 disclose a double role of the amorphous surface in this reaction. The equilibrium between the surface hydroxyls and $H_2O_{2(aq)}$ leads to the formation of surface HO_2^- anions (Equations (7)-(8)), constituting the first step of H_2O_2 decomposition. The second role of *a*-ZrO_2 was revealed by analyzing the amount of the produced hydroxyl radicals as a function of the pH value. As implied by Figure 9, apparently it varies in a parallel way with the content of the superoxide radicals, implying that during H_2O_2 decomposition these both intermediates are produced simultaneously. This mechanistically crucial observation rules out the homolytic splitting of H_2O_2 into the hydroxyl radicals (Equation 1), proposed earlier for crystalline ZrO_2 oxides,[26,27,28] since in this mechanism $HO_2^\bullet$ (and $O_2^{-\bullet}$) species are formed at the expense of the hydroxyl radicals (Equation (2)). The observed concomitant formation of $^\bullet OH$ and $O_2^{-\bullet}$ species with the same pH-dependency (Figure 9a,b) implies the following electroprotic reaction to be involved:

$$\equiv Zr^+–HO_2^-{}_{(surf)} + H_2O_{2(aq)} \rightarrow {}^\bullet OH_{(aq)} + \equiv Zr^+–O_2^{-\bullet}{}_{(surf)} + H_2O. \qquad (9)$$

It can be regarded as the ionic equivalent of the Haber-Weiss reaction ($HO_2^\bullet + H_2O_2 = OH^\bullet + O_2 + H_2O$)[55] induced by the ionic sponge effect (strong electrostatic stabilization of the charged superoxide ions on the tetravalent zirconium ≡Zr(IV) centers of the amorphous zirconia gel). Due to the coupled proton and electron transfer it can formally be envisaged as transfer of a hydrogen atom ($H^\bullet$ (p^+/e^-) + H_2O_2 = $^\bullet OH$ + H_2O) released from the HO_2^- moiety. It is worth mentioning that akin hydrogen transfer processes have been postulated for H_2O_2 decomposition previously.[56]

For the analogous reaction in the liquid phase ($HO_2^-{}_{(aq)} + H_2O_{2(aq)} = {}^\bullet OH_{(aq)} + O_2^{-\bullet}{}_{(aq)} + H_2O$), the thermodynamic calculations, based on the averaged values of the redox potentials of the corresponding partial reactions available from literature (see Supporting Information), give the $\Delta_r G^\circ$ value around 15 kcal/mol. Such positive value is caused by weak dissociation constant of H_2O_2 ($K_a = 2\times10^{-12}$), and low stability of the superoxide anion in the aqueous environment. Thus, the unfavorable thermodynamics has to be overcome by engagement of the gel surface for stabilization of the ionic intermediates (HO_2^- and $O_2^{-\bullet}$). From the observed g_{zz} value of the superoxide species trapped on the Zr(IV) sites, the stabilization energy of the adsorbed $O_2^{-\bullet}$ can be estimated,[57] which amounts to about 0.9 eV, driving the above electroprotic reactions toward formation of the superoxide and hydroxyl radicals.

At pH < IEP, surface is charged positively by protonation, favoring stabilization of the anionic species as counter ions. Above IEP, the negative potential of the surface disfavors trapping of the superoxide anions making the whole process not only pH-dependent but also IEP-dependent. Furthermore, deprotonation of the surface HO_2^- species (*vide infra*) quenches all the electroprotic processes. The decreasing $O_2^{-\bullet}$ trapping efficiency of the zirconia surface with the increasing pH value above IEP accounts for the observed concomitant decline of the superoxide and hydroxyl radical formation. The proposed mechanism explains also the crucial role of the zirconia phase in the H_2O_2 decomposition. In contrast to crystalline ZrO_2, only in the amorphous state of zirconia, its surface area (Figure 4a) and the amount of terminal hydroxyl groups are sufficiently large to promote effectively the reaction described by Equation (9).

It is also worth noting that analogous radical products were observed for reaction between *a*-ZrO_2 and H_2O_2 carried out in a dry phase (adsorption of gaseous H_2O_2, produced by thermal decomposition of $CO(NH_2)_2 \cdot H_2O_2$ substrate, on the surface of *a*-ZrO_2 pre-impregnated with DMPO for ${}^\bullet OH$ detection by EPR). Thus, it implies that reaction (9) proceeds regardless the presence of aqueous medium, and that the crucial role is played by the ability of H_2O_2 to ligate to the gel surface:

$$2H_2O_{2(aq)} + \equiv Zr–OH_{(surf)} + DMPO_{(surf)} \rightarrow {}^\bullet OH–DMPO_{(surf)} + \equiv Zr^+–O_2^{-\bullet}{}_{(surf)} + 2H_2O. \qquad (10)$$

An alternative radical mechanism of $O_2^{-\bullet}$ formation via deprotonation of the hydroperoxyl radical,[58] produced according to the reactions (1) and (2),

$$HO_2^\bullet{}_{(aq)} \rightarrow H^+{}_{(aq)} + O_2^{-\bullet}{}_{(surf)}, \qquad (11)$$

can be disregarded as the observed concordance between the formation of $O_2^{-\bullet}$ and $OH^\bullet$ (shown in Figure 8) is lost, for the intermediate $HO_2^\bullet$ radicals may decay in a parallel route described by Equation (3). Furthermore, in the low pH region the deprotonation equilibrium (11), for which $pK_a = 4.8$,[59] in an aqueous medium will be strongly shifted to the left. Although the EPR signals of the superoxide radicals formed on the surface of crystalline[26] and amorphous zirconia samples are virtually identical in shape, they differ dramatically in the intensity (1:60) implying that the involved mechanisms must be different. According to the postulated reaction steps (1), (2) and (11), one may expect that rate of decomposition of H_2O_2 via homolytic HO–OH bond splitting is proportional to concentration of $O_2^{-\bullet}$ and reversibly proportional to [$^{\bullet}$OH]. This remains in variance with our experimental results shown in Figure 9. It should be noted, however, that the mechanisms based on the homolytic HO–OH bond splitting may operate in a feeble way at the background being dominated by the electroprotic pathway. The proportion of involvement of both mechanisms may vary with the nature of gel catalysts used for H_2O_2 decomposition.

In contrast to the non-monotonous profile of the $O_2^{-\bullet}$ formation, the surface peroxy anions are produced steadily with the increasing pH implying a simple pathway that may involve formation of bridging peroxo groups:

$$H_2O_{2(aq)} + 2(\equiv Zr–O^{-}_{(surf)}) \rightarrow \equiv Zr^{+}–O_2^{2-}–{}^{+}Zr\equiv_{(surf)} + 2OH^{-}_{(aq)}, \qquad (12)$$

or bidentate peroxo groups:

$$H_2O_{2(aq)} + \equiv Zr–O^{-}_{(surf)} \rightarrow \equiv Zr^{+}–O_2^{2-}{}_{(surf)} + H_2O. \qquad (13)$$

Both reactions are driven by stabilization of the resultant O_2^{2-} anionic species at the surface of the amorphous zirconia in form of the μ-peroxide or η^2-peroxide complexes, respectively. Such adsorption species have been described in the zirconia-based systems[45] as well other supported systems active in H_2O_2 decomposition.[2] The crucial role in these processes is played by high charge of the Zr(IV) surface cations and that of the O_2^{2-} species as well. Due to the sizeable electrostatic interactions the dianions O_2^{2-} can be trapped at the surface more effectively, replacing the monoanionic $O_2^{-\bullet}{}_{(surf)}$ or $OH^{-}_{(surf)}$ species.

3.4. Peroxidase- and catalase-like activity

It has been found previously that redox oxides such as Co_3O_4,[33] MnO_2,[60] or some metals[61] can exhibit both the catalase and the peroxidase types of activity in H_2O_2 decomposition. Thus, we examined these types of reactivity toward hydrogen peroxide in the case of the non-redox amorphous zirconia catalyst.

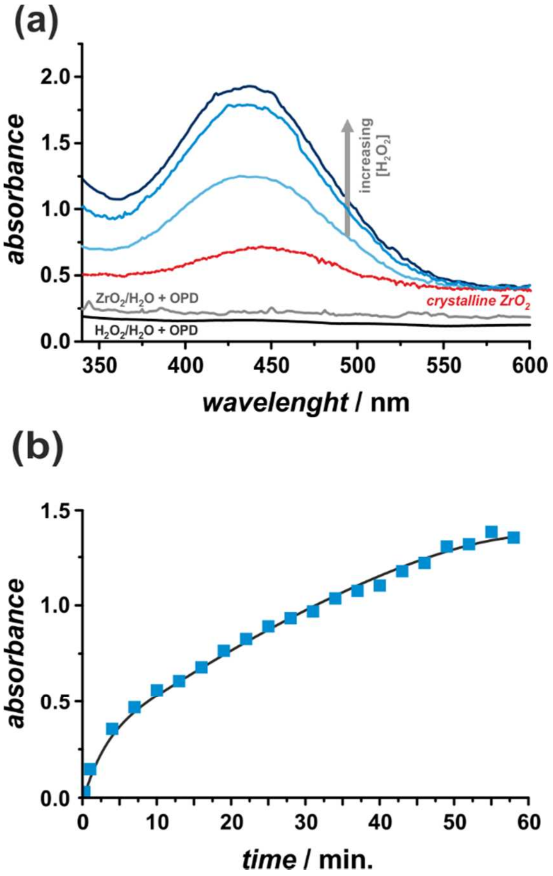

Figure 10. (a) Absorption UV-Vis spectra of *a*-ZrO_2 – H_2O_2/H_2O suspension in presence of OPD substrate with increasing amount of H_2O_2 (red line represents analogous spectrum for crystalline *m*-ZrO_2), and (b) changes in the intensity of the 440 nm band with time. The concentration of H_2O_2 in the reaction mixture equals to 0.3, 0.6 and 0.9 mol/L, concentration of OPD is 1.2 mmol/L, and the amount of ZrO_2 is 1.3 mg/mL. The kinetic curve (accumulated amount of the hydroxyl radicals produced versus time) corresponds to $[H_2O_2] = 0.3$ mol/L.

Peroxidase-like activity of *a*-ZrO_2 (formation of hydroxyl radicals in the liquid part of the suspension) was investigated using OPD substrate. After admission of an amorphous zirconia sample to aqueous solution of H_2O_2 in the presence of OPD, the color of the reaction mixture changes into orange, and a characteristic band in the UV-Vis spectrum at 440 nm, assigned to 2,3-diaminophenazine (an oxidation product of OPD by the evolving $^{\bullet}OH$ radicals), appeared (Figure 10a). Blank experiments performed in the absence of *a*-ZrO_2 or H_2O_2 revealed that such band does not appear. The intensity of the 440 nm band increases with time (Figure 10b), monitoring the progress of the H_2O_2 decomposition that involves formation of the hydroxyl radical intermediates (accumulated amount of the hydroxyl radicals produced versus time). In agreement with earlier studies,[28a,b] also the crystalline ZrO_2 shows some activity in this reaction (Figure 10a, red line), however, the observed absorbance is only 30% of that obtained for the amorphous sample (both experiments were carried out with $[H_2O_2] = 0.3$ mol/L and the absorbance is normalized to the mass of the catalysts in crystalline phase).

Parallel tests of H_2O_2 decomposition over *a*-ZrO_2 in the presence of NBT substrate (specific for superoxide radicals) failed to reveal the presence of any $O_2^{-\bullet}$ species in the liquid phase, in agreement with the spin trapping EPR measurements. This confirms once more that all the generated superoxide radicals are essentially captured by the amorphous zirconia surface, and that the reaction (9) can only proceed at the interface of the H_2O_2 solution and the surface of *a*-ZrO_2. As a consequence, the surface of the catalyst was colored dark blue due to the adsorption of NBT and its subsequent oxidation by the surface-stabilized superoxide species, while the supernatant remained colorless. This observation, again, remains in agreement with the spin trapping experiments.

To verify catalase-like activity of the amorphous ZrO_2 we examined production of dioxygen as a product of H_2O_2 decomposition. The amount of the produced dioxygen, dissolved in water, as a function of the reaction time and pH of the suspension is shown in Figure 11. As expected, concentration of the dissolved oxygen and its production rate increase with pH of the solution. However, comparison of the O_2 concentration profiles obtained in the presence and absence of ZrO_2 catalysts (see Supporting Information, Figure S4) indicates that the amount of the dissolved O_2 is higher when zirconia is involved for each of the investigated pH values. Thus, again the amorphous ZrO_2 plays a catalytic role in this reaction. At pH > 5.3 hydrogen peroxide undergoes predominantly decomposition into O_2, and the superoxide production drops dramatically (Figure 9a). Thus, its role as a source of ROS is declined. This pH range favors catalase-like reactivity of *a*-ZrO_2, where H_2O_2 is decomposed into O_2 with pronounced attenuation of the ROS intermediates generation, which is unfavorable for catalytic purposes.

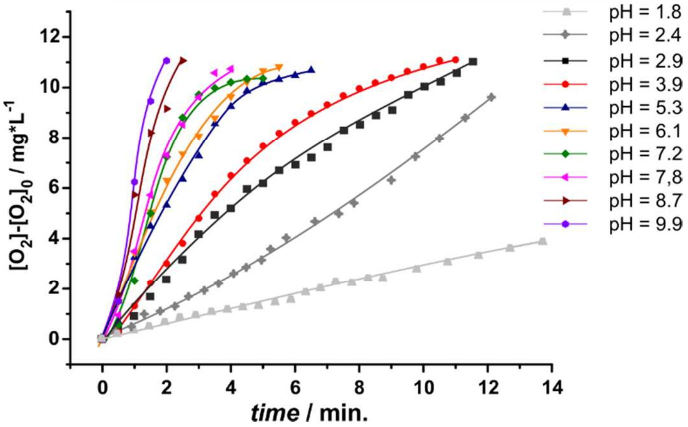

Figure 11. Evolution of dissolved dioxygen produced during decomposition of H_2O_2 over *a*-ZrO_2. The concentration of H_2O_2 is 0.06 mol/L, the amount of *a*-ZrO_2 is 23 mg per 150 mL of the solution, the reaction temperature is 295 K.

Below pH of 5.3 decomposition into O_2 is slow, and production of the $^{\bullet}OH$ and $O_2^{-\bullet}$ radicals dominates, being benign for catalytic oxidation reactions. Indeed, the presence of the hydroxylated ZrO_2 gel, which exhibits ionic sponge properties, triggers the interfacial ionic and the aqueous-phase radical reactions resembling the peroxidase-like activity.

In order to prove the peroxidase-type activity of the amorphous ZrO_2 definitely, a comparison with the activity of the horseradish peroxidase (HRP) was carried out. As a simple activity measure the Michaelis-Menten constant, K_m, was calculated for the OPD oxidation reaction

$$1/v = K_m/V_m(1/[S] + 1/K_m), \qquad (14)$$

where v is the initial reaction rate, V_m – maximal reaction rate, and [S] is the concentration of the substrate. For the sake of direct comparison with HRP performance, the reaction between *a*-ZrO_2 and H_2O_2 was carried out at pH = 4. The literature value of the Michaelis-Menten constant for HRP (3.7 mM)[62] is substantially smaller than that obtained for *a*-ZrO_2 (K_m = 62.2 mM), which means that the amorphous zirconia is much more active that the reference enzyme used for the activity benchmarking. The peroxidase-like activity of *a*-ZrO_2 reaches almost half of the values characteristic of typical redox oxides (K_m = 154.0 mM for Fe_3O_4 and 140.7 mM for Co_3O_4),[62] for which direct redox mechanism operates, indicating the importance of the new mechanism proposed in this study in efficient generation of the hydroxyl radicals.

A correlation between the initial rate of dioxygen release $v(O_2)$ and the amount of the produced $^{\bullet}OH$ radicals as a function of pH is shown in Figure 12. The quadrant for which $[^{\bullet}OH] > 0.5$ and $v(O_2) < 0.5$ (marked in green in Figure 12) can be identified with the peroxidase-like activity, while the catalase-like activity corresponds to the opposite quadrant (marked in yellow).

The diagram shown in Figure 12 may be applied as a conceptual framework for interpretation of the catalytic processes where H_2O_2 is used as the oxidant. The peroxidase-type activity may be regarded as a measure of preferable generation of abundant hydroxyl intermediates that can be used for the oxidation processes, whereas the catalase-like activity corresponds to that part of H_2O_2 which is practically lost by immediate decomposition into dioxygen with only minor formation of the chemically valuable ROS transients.

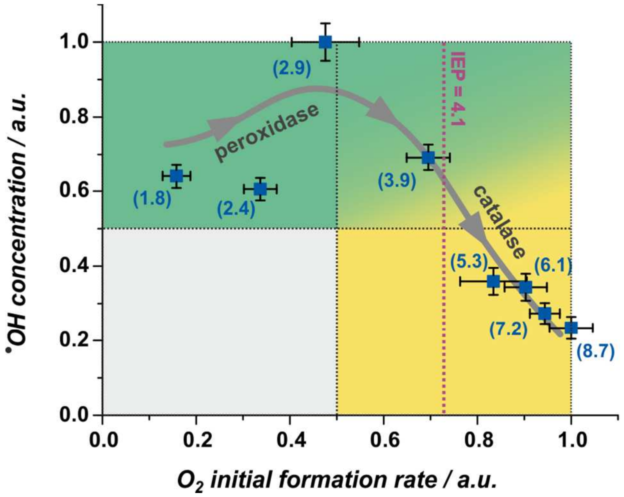

Figure 12. Correlation between O_2 formation rate and concentration of $^{\bullet}OH$ radicals. The initial O_2 production rates were obtained from the slopes of the curves shown in Figure 11, whereas the hydroxyl radicals were quantified by means of the UV-Vis measurements (Figure 10). The numbers in the parentheses correspond to the actual pH values.

3.5. Catalytic implications

For designing a catalytic system based on ZrO_2 for oxidation reactions with H_2O_2, the pH value plays a crucial role as it controls the amount and the kind of the generated reactive oxygen species. The preferable experimental conditions correspond to pH value just below IEP. The amorphous form of zirconia is much more active than the crystalline phases due to the combined effect of surface area and extended surface hydroxylation. Because at high pH values the ability for generation of hydroxyl radicals dramatically decreases, a shift to the beneficial pH range may be accomplished by using binary gels with acidic components such as ZrO_2-SiO_2, which are active in oxidation of cyclohexene with H_2O_2.[63] In the basic conditions O_2^{2-} may be used as the oxidizing species, as exemplified by epoxidation reactions.[10e,64] However, such conditions favor unproductive vanishing of hydrogen peroxide, lowering the stoichiometric efficiency of the oxidation reaction.

It is also expected that zirconia gel and akin catalysts, in contrast to Fenton (redox) catalysts, lead to a more uniform generation of hydroxyl radicals in time. In the case of redox systems, which are based on electron transfer, the $^{\bullet}OH$ radicals are formed upon immediate dissociation of the transient $H_2O_2^{-}$ due to its very shallow potential energy surface.[65] In the case of d^0 oxide gel catalysts, production of the hydroxyl radicals occurs in a more uniform way, since the involved mechanism exhibit a multistep character (reactions (7) – (9)), engaging interfacial relocation of electrons, protons, and ions. The d^0 gel catalysts may also be of the potential interest in oxidative treatment of contaminated water at circumneutral pH values, since their isoelectric point can be appropriately adjusted by formation of binary gels such as ZrO_2-Al_2O_3, ZrO_2-Y_2O_3 (the work in this direction is in progress).

The obtained results show clearly that the activity of the amorphous ZrO_2 in decomposition of H_2O_2 results from complex electroprotic processes ranging from catalase- to peroxidase-like behavior, where the surface of *a*-ZrO_2 plays an important role of the ionic sponge. The nature of the generated ROS varieties can be easily controlled by mere pH changes, which allows for simple tuning of the catalysts activity to the desired specific applications. Furthermore, the proposed mechanism of ROS formation (reaction (9)) may have important implications for understanding not only the catalytic processes involving H_2O_2 but also for their appearance in biological and environmental systems, where amorphous non-redox oxide gels are present. However, it does not disregard the previous mechanisms based on homolytic HO–OH bond splitting[26,27,28] to operate in a parallel, latent way (with far less contribution in the case of zirconia gel).

4. Conclusions

Despite the non-redox nature of amorphous ZrO_2, its interaction with H_2O_2 results in formation of several reactive oxygen species, such as $^{\bullet}OH$, $O_2^{-\bullet}$, and O_2^{2-} in the amounts comparable to those observed for the typical Fenton-type oxides. ROS were detected by EPR/HYSCORE techniques complemented with Raman, XPS, and TG-MS measurements. It was found that both hydroxyl and superoxide radicals were formed simultaneously according to the electroprotic mechanism, where the following equilibrium $\equiv Zr^{+}–HO_2^{-}{}_{(surf)} + H_2O_{2(aq)} \rightarrow {}^{\bullet}OH_{(aq)} + \equiv Zr^{+}–O_2^{-\bullet}{}_{(surf)} + H_2O$ plays a central role. In the postulated mechanism an electron transfer occurs between the $H_2O_{2(aq)}$ and $HO_2^{-}{}_{(surf)}$ species without direct engagement of ZrO_2. The amorphous state of ZrO_2 substrate is beneficial since the latter acts as the ionic sponge for trapping the charged $O_2^{-\bullet}$, O_2^{2-} species and protons. Speciation of the ROS intermediates depends on pH of the solution and the isoelectric point of the gel oxide catalyst. At pH below 5.3 the superoxide and hydroxyl radicals were generated simultaneously in large amounts, whereas above this value formation of O_2^{2-} was accompanied by a substantial release of O_2. While crystalline ZrO_2 exhibited poor activity in simultaneous generation of $^{\bullet}OH$ and $O_2^{-\bullet}$ radicals, the amorphous zirconia was far more active, owing to the combined effect of the high surface area and extended hydroxylation. Depending on pH, hydrogen peroxide can be decomposed along the peroxidase- or catalase-like pathways over amorphous ZrO_2. The reactivity of zirconia gel in ROS formation via H_2O_2

decomposition was rationalized in terms of a diagram showing correlation between formation rate of dioxygen $v(O_2)$ versus hydroxyl radical concentration [$^\bullet$OH].

Corresponding Author

* Piotr Pietrzyk, Faculty of Chemistry, Jagiellonian University, ul. R. Ingardena 3, 30-060 Krakow, POLAND, tel. +48 12 663 22 24, fax. +48 12 634 05 15, e-mail: pietrzyk@chemia.uj.edu.pl, piotr.pietrzyk@uj.edu.pl

Notes

The authors declare no competing financial interest.

Supporting Information

The Supporting Information is available free of charge on the ACS Publications website. Experimental details on pulse EPR measurements and simulated HYSCORE spectra, calculation of $\Delta_r G°$ for ROS formation reaction from available literature data, additional XPS data, IEP measurements, dissolved O_2 concentration profiles for H_2O_2/H_2O solutions. This material is available free of charge via the Internet at http://pubs.acs.org.

ACKNOWLEDGMENT

National Science Center (NCN) of Poland is acknowledged for the financial support of this work (Grant No. 2015/17/N/ST5/01956). The research was carried out with the equipment purchased thanks to the financial support of the European Regional Development Fund in the framework of the Polish Innovation Economy Operational Program (contract no. POIG.02.01.00-

12-023/08). Authors wish to thank Professor Mario Chiesa (University of Turin) for his help in the pulse EPR experiments.

REFERENCES

---

(1) An, Q.; Sun, C.; Li, D.; Xu, K.; Guo, J.; Wang, C. *ACS Appl. Mater. Interface.* **2013**, *24*, 13248–13257.

(2) Bokare, A. D.; Choi, W. *J. Hazard. Mater.* **2014**, *275*, 121–135.

(3) Mu, J.; Zhang, L.; Zhao, M.; Wang, Y. *J. Mol. Catal. A: Chemical* **2013**, *378*, 30–37.

(4) Yoon, C. W.; Hirsekorn, K. F.; Neidig, M. L.; Yang, X.; Tilley, T. D. *ACS Catal.* **2011**, *1*, 1665–1678.

(5) Ziółek, M.; Sobczak, I.; Decyk, P.; Sobańska, K.; Pietrzyk, P.; Sojka, Z. *Appl. Catal. B: Environ.* **2015**, *164*, 288–296.

(6) Yang, M.; Zhang, X.; Grosjean, A.; Soroka, I.; Jonsson, M. *J. Phys. Chem. C* **2015**, *119*, 22560−22569.

(7) Oszajca, M.; Brindell, M.; Orzeł, Ł.; Dąbrowski, J. M.; Śpiewak, K.; Łabuz, P.; Pacia, M.; Stochel-Gaudyn, A.; Macyk, W.; van Eldik, R.; Stochel, G. *Coord. Chem. Rev.* **2016**, *327-328*, 143–165.

(8) Zasada, F.; Piskorz, W.; Janas, J.; Gryboś, J.; Indyka, P.; Sojka, Z. *ACS Catal.* **2015**, *5*, 6879–6892.

(9) Cooper, W. J.; Cramer, C. J.; Martin, N. H.; Mezyk, S. P.; O'Shea, K. E.; Von Sonntag, C. *Chem. Rev.* **2009**, *109*, 1302–134.

---

(10) (a) Thornburg, N. E.; Thompson, A. B.; Notestein, J. M. *ACS Catal.* **2015**, *5*, 5077−5088, (b) Ottenbacher, R. V.; Samsonenko, D. G.; Talsi, E. P.; Bryliakov, K. P. *ACS Catal.* **2014**, *4*, 1599−1606, (c) Lyakin, O. Y.; Ottenbacher, R. V.; Bryliakov, K. P.; Talsi, E. P. *ACS Catal.* **2012**, *2*, 1196−1202, (d) Huang, J.; Akita, T.; Faye, J.; Fujitani, T.; Takei, T.; Haruta, M. *Angew. Chem., Int. Ed.* **2009**, *48*, 7862–7866, (e) Chen, C.; Yuan, H.; Wang, H.; Yao, Y.; Ma, W.; Chen, J.; Hou, Z. *ACS Catal.* **2016**, *6*, 3354–3364.

(11) (a) Saisaha, P.; Dong, J. J.; Meinds, T. G.; de Boer, J. W.; Hage, R.; Mecozzi, F.; Kasper, J. B.; Browne, W. R. *ACS Catal.* **2016**, *6*, 3486−3495, (b) Shima, H.; Tanaka, M.; Imai, H.; Yokoi, T.; Tatsumi, T.; Kondo, J. N. *J. Phys. Chem. C* **2009**, *113*, 21693–21699.

(12) (a) Gogate, P. R.; Pandit, A. B. *Adv. Environ. Res.* **2004**, *8*, 501–551, (b) Pignatello, J. J.; Oliveros, E.; MacKay, A. *Crit. Rev. Environ. Sci. Technol.* **2006**, *36*, 1–84, (c) Sheng, J.; Li, X.; Xu, Y. *ACS Catal.* **2014**, *4*, 732−737.

(13) Liang, Y. T.; Lin, S. P.; Liu, C. W.; Chung, S. R.; Chen, T. Y.; Wang, J. H.; Wang, K. W. *Chem. Commun.* **2015**, *51*, 6605–6608.

(14) Danilczuk, M.; Coms, F. D.; Schlick S. *Macromolecules* **2009**, *42*, 8943–8949.

(15) Trogadas, P.; Parrondo, J.; Ramani, V. *Electrochem. Solid-State Lett.* **2008**, *11*, B113–B116.

(16) Raffellini, S.; Schenk, M.; Guerrero, S.; Alzamora, S. M. *Food Control* **2011**, *22*, 920–932.

---

(17) Cieślik, M.; Zimowski, S.; Gołda, M.; Engvall, K.; Pan, J.; Rakowski, W.; Kotarba, A. *Mater. Sci. Eng. C* **2012**, *32*, 2431–2435.

(18) Prasad, A. K.; Mishra, P. C. *J. Phys. Chem. B* **2015**, *119*, 7825–7836.

(19) Do, S. H.; Batchelor, B.; Lee, H. K.; Kong, S. H. *Chemosphere* **2009**, *75*, 8–12.

(20) (a) Novara, C.; Alfayate, A.; Berlier, G.; Maurelli, S.; Chiesa, M. *Phys. Chem. Chem. Phys.* **2013**, *15*, 1099–11105. (b) Clerici, M. G. In *Metal Oxide Catalysis*, Jackson, D., Hargreaves, J. S. J., Eds.; Wiley-VCH Verlang GmbH & Co. KGaA: Weinheim, Germany, 2008; pp 705–754, (c) Alba-Rubio, A. C.; Fierro, J. L. G.; León-Reina, L.; Mariscal, R.; Dumesic, J. A.; López Granados, M. *Appl. Catal. B: Environ.* **2017**, *202*, 269–280, (d) Lu, X.; Wu, H.; Jiang, J.; He, M.; Wu, P. *J. Catal.* **2016**, *342*, 173–183.

(21) Forde, M. M.; Armstrong, R. D.; Hammond, C.; He, Q.; Jenkins, R. L.; Kondrat, S. A.; Dimitratos, N.; Lopez-Sanchez, J. A.; Taylor, S. H.; Willock, D.; Kiely, C. J.; Hutchings, G. J. *J. Am. Chem. Soc.* **2013**, *135*, 11087−11099.

(22) Hammond, C.; Forde, M. M.; Rahim, M. H. A.; Thetford, A.; He, Q.; Jenkins, R. L.; Dimitratos, N.; Lopez-Sanchez, J. A.; Dummer, N. F.; Murphy, D. M.; Carley, A. F.; Taylor, S. H.; Willock, D. J.; Stangland, E. E.; Kang, J.; Hagen, H.; Kiely, C. J.; Hutchings, G. J. *Angew. Chem., Int. Ed.* **2012**, *51*, 5129–5133.

(23) Hammond, C.; Dimitratos, N.; Jenkins, R. L.; Lopez-Sanchez, J. A.; Kondrat, S. A.; Ab Rahim, M. H.; Forde, M. M.; Thetford, A.; Taylor, S. H.; Hagen, H.; Stangland, E. E.; Kang, J.; Moulijn, J. M.; Willock, D. J.; Hutchings, G. J. *ACS Catal.* **2013**, *3*, 689–699.

(24) Keshavaraja, A.; Ramaswamy, V.; Soni, H. S.; Ramaswamy, A. V.; Ratnasamy, P. *J. Catal.* **1995**, *157*, 501–511.

(25) Ziolek, M.; Sobczak, I.; Decyk, P.; Wolski, L. *Catal. Comm.* **2013**, *37*, 85–91.

(26) (a) Giamello, E.; Volante, M.; Fubini, B.; Geobaldo, F.; Morterra, C. *Mater. Chem. Phys.* **1991**, *29*, 379–386, (b) Giamello, E.; Calosso, L.; Fubini, B.; Geobaldo, F. *J. Phys. Chem.* **1993**, *97*, 5735–5740, (c) Giamello, E.; Rumori, P.; Geobaldo, F.; Fubini, B.; Paganini, M. C. *Appl. Magn. Reson.* **1996**, *10*, 173–192.

(27) Hiroki, A.; LaVerne, J. A. *J. Phys. Chem. B* **2005**, *109*, 3364–3370.

(28) (a) Lousada, C. M.; Jonsson, M. *J. Phys. Chem. C* **2010**, *114*, 11202–11208, (b) Lousada, C. M.; Johansson, A.; Brinck, T.; Jonsson, M. *J. Phys. Chem. C* **2012**, *116*, 9533–9543, (c) Lousada, C. M.; LaVerne, J. A.; Jonsson, M. *Phys. Chem. Chem. Phys.* **2013**, *15*, 12674–12679.

(29) Novikov, A. S.; Kuznetsov M. L.; Pombeiro A. J. L.; Bokach, N. A.; Shul'pin, G. B. *ACS Catal.* **2013**, *3*, 1195−1208.

(30) Rhee, S. G.; Yang, K.-S.; Kang, S. W.; Woo, H. A.; Chang, T.-S. *Antioxid. Redox Sign.* **2005**, *7*, 619–626.

(31) Zong, S.; Cao, Y.; Zhou, Y.; Ju, H. *Langmuir* **2006**, *22*, 8915–8919.

(32) Zhang, L.; Han, L.; Peng, H.; Wang, L.; Dong, S. *Chem. Commun.* **2013**, *49*, 10480–10482.

(33) Mu, J.; Wang, Y.; Zhao, M.; Zhang, L. *Chem. Commun.* **2012**, *48*, 2540–2542.

(34) Gao, L.; Zhuang, J.; Nie, L.; Zhang, J.; Zhang, Y.; Gu, N.; Wang, T.; Feng, J.; Yang, D.; Perrett, S.; Yan, X. *Nat. Nanotechnol.* **2007**, *2*, 577–583.

(35) André, R.; Natálio, F.; Humanes, M.; Leppin, J.; Heinze, K.; Wever, R.; Schröder, H. C.; Müller, W. E. G.; Tremel, W. *Adv. Funct. Mater.* **2011**, *21*, 501–509.

(36) Asati, A.; Santra, S.; Kaittanis, C.; Nath, S.; Perez, J. M. *Angew. Chem., Int. Ed.* **2009**, *48*, 2308–2312.

(37) Dai, Z.; Liu, S.; Bao, J.; Ju, H. *Chem. Eur. J.* **2009**, *15*, 4321–4326.

(38) (a) Josephy, P. D.; Eling, T.; Mason, R. P. *J. Biol. Chem.* **1982**, *257*, 3669–3675, (b) Al-Kaissi, E.; Mostratos, A. *J. Immunol. Meth.* **1983**, *58*, 127–132.

(39) Prasanna, V. L.; Vijayaraghavan, R. *Langmuir* **2015**, *31*, 9155–9162.

(40) Buettner, G. R. *Free Radical Biol. Med.* **1987**, *3*, 259–303.

(41) Spalek, T.; Pietrzyk, P.; Sojka, Z. *J. Chem. Inf. Model.* **2005**, *45*, 18–29.

(42) Stoll, S.; Schweiger, A. *J. Magn. Reson.* **2006**, *178*, 42–55.

(43) Park, J. H.; Oh, J. Y.; Han, S. W.; Lee, T. I.; Baik, H. K. *ACS Appl. Mater. Interfaces* **2015**, *7*, 4494−4503.

(44) (a) Sala-Pala, J.; Roue, J.; Guerchais, J. E. *J. Mol. Catal.* **1980**, *7*, 141–148, (b) Bayot, D.; Devillers, M. *Coord. Chem. Rev.* **2006**, *250*, 2610–2626, (c) Cardoso, F. P.; Nogueira, A. E.; Patrício, P. S. O.; Oliveira, L. C. A. *J. Brazil. Chem. Soc.* **2012**, *23*, 702–709, (d) Wachs, E. I. Ch.; Roberts, A. *Chem. Soc. Rev.* **2010**, *39*, 5002–5017.

(45) Faccioli, F.; Bauer, M.; Pedron, D.; Soraràù, A.; Carraro, M.; Gross, S. *Eur. J. Inorg. Chem.* **2015**, 210–225.

(46) Sobańska, K.; Krasowska, A.; Mazur, T.; Podolska-Serafin, K.; Pietrzyk, P.; Sojka, Z. *Top. Catal.* **2015**, *58*, 796–810.

(47) Schweiger, A.; Jeschke, G. *Principles of Pulse Electron Paramagnetic Resonance*, Oxford University Press: Oxford, U.K., 2001.

(48) Pöppl, A.; Kevan, L. *J. Phys. Chem*. **1996**, *100*, 3387–3394.

(49) Jeschke, G.; Rakhmatullin, R.; Schweiger, A. *J. Magn. Reson.* **1998**, *131*, 261–271.

(50) Añez, R.; Sierraalta, A.; Martorell, G.; Sautet, P. *Surf. Sci.* **2009**, *603*, 2526–2531.

(51) Jakubus, P.; Adamski, A.; Kurzawa, M.; Sojka, Z. *J. Therm. Anal. Calorim.* **2003**, *72*, 299–310.

(52) Sojka Z.; Che M. *Top. Catal.* **2001**, *15*, 211–217.

(53) (a) Clearfield, A. *Chem. Rev.* **1988**, *88*, 125–148, (b) England, W. A.; Cross, M. G.; Hamnett, A.; Wiseman, P. J.; Goodenough, J. B. *Solid State Ionics* **1980**, *1*, 231–249.

(54) Zhang, G.; Kim, G.; Choi, W. *Energy Environ. Sci.* **2014**, *7*, 954–966.

(55) Weinstein, J.; Bielski, B. H. J. *J. Am. Chem. Soc.* **1979**, *101*, 58–62.

(56) Lin, S.-S.; Gurol, M. D. *Environ. Sci. Catal.* **1998**, *32*, 1417–1423.

(57) Dyrek, K.; Adamski, A.; Sojka, Z. *Spectrochmica Acta Part A* **1998**, *54*, 2337–2348.

---

(58) Antcliff, K. L.; Murphy, D. M.; Griffiths, E.; Giamello, E. *Phys. Chem. Chem. Phys.* **2003**, *5*, 4306–4316.

(59) Behar, D.; Czapski, G.; Rabani, J.; Dorfman, L. M.; Schwarz, H. A. *J. Phys. Chem.* **1970**, *74*, 3209–3211.

(60) Liu, X.; Wang, Q.; Zhao, H.; Zhang, L.; Sub, Y.; Lv, Y. *Analyst* **2012**, *137*, 4552–4558.

(61) Li, J.; Liu, W.; Wu, X.; Gao, H. *Biomaterials* **2015**, *48*, 37–44.

(62) Niu, X.; Xu, Y.; Dong, Y.; Qi, L.; Qi, S.; Chen, H.; Chen, X. *J. Alloy. Compd.* **2014**, *587*, 74–81.

(63) Morandin, M.; Gavagnin, R.; Pinna, F.; Strukul, G. *J. Catal.* **2002**, *212*, 193–200.

(64) Somma, F.; Canton, P.; Strukul, G. *J. Catal.* **2005**, *229*, 490–498.

(65) (a) Nandi, D.; Krishnakumar, E.; Rosa, A.; Schmidt W.-F.; Illenberger, E. *Chem. Phys. Lett.* **2003**, *373*, 454–459, (b) Hrušák, J.; Friedrichs, H.; Schwarz, H.; Razafinjanahary, H.; Chermette, H. *J. Phys. Chem.* **1996**, *100*, 100–110.

TOC

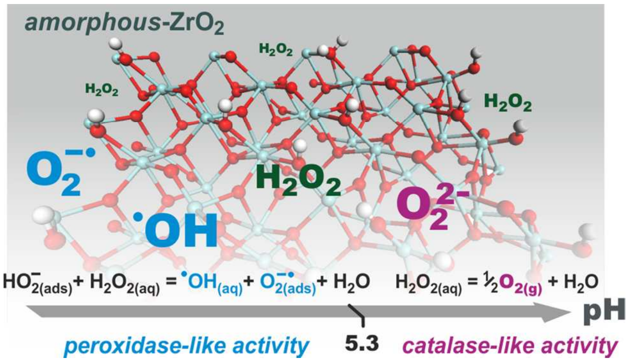
amorphous-ZrO_2
H_2O_2
H_2O_2
H_2O_2
$O_2^{-\bullet}$
H_2O_2
$^{\bullet}OH$
O_2^{2-}
$HO^-_{2(ads)} + H_2O_{2(aq)} = {}^{\bullet}OH_{(aq)} + O^{-\bullet}_{2(ads)} + H_2O$
$H_2O_{2(aq)} = \frac{1}{2}O_{2(g)} + H_2O$
pH
5.3
peroxidase-like activity
catalase-like activity